Supporting Information

Zhang et al. 10.1073/pnas.1209893109

SI Materials and Methods

Atomic Force Microscopy Indentation Measures the Relative Mechanical Difference Between MCF-7/GFP and MDA-MB-436/RFP Cell Lines. A Bioscope II atomic force microscope (AFM) (Bruker, formerly Veeco) combined with a fluorescence microscope (Nikon TE-2000 inverted optical microscope) was used in this study. The colloidal AFM probe had a 5-μm diameter borosilicate glass particle attached at the tip of silicon nitride V-shaped cantilevers (Novascan). Data were acquired and analyzed with NanoScope software (v1.40; Bruker). The cantilever spring constant was calibrated using thermal tuning and generated values ranging from 0.1 to 0.25 N/m, with less than 8% error, in cell-culture medium (nominal value of 0.24 N/m). Two sets of AFM indentation tests were carried out. The first test was with a ramp size of 2 μm and ramp velocity of 2 μm/s. The second test was with a ramp size of 500 nm and velocity of 500 nm/s. The same trigger threshold (1V or 12.69 nN) was used for the both AFM indentation tests. Fig. S1 shows the AFM tip approaching cells in a typical indentation test.

The force-distance curve was analyzed with the NanoScope software. The indentation function of NanoScope provides various indentation models to fit measured force curves and calculate Young's modulus. Following the Hertz model (spherical indenter), Eq. S1 was used to calculate Young's modulus. Fig. S2 shows a typical force-distance curve and the fitted force curve, with related input parameters.

$$F = \frac{4}{3}\frac{E}{(1-\upsilon^2)}\sqrt{R}\delta^{\frac{3}{2}} \qquad \textbf{[S1]}$$

Eq. **S1** is a Hertz model, where F = force (from force curve), E = Young's modulus (fit parameter), ν = Poisson's ratio [0.5 was used (1)], R = radius of the indenter, δ = indentation.

Fig. S3 shows the estimated Young's moduli of MCF-7/GFP and MDA-MB-436/RFP cells, tested with ramp sizes of 2 μm (Fig. S3*A*) and 500 nm (Fig. S3*B*). Together, both sets of data show that MDA-MB-436/RFP cells have the higher estimated Young's moduli.

There is still debate about AFM-based Young's modulus calculation in living cells (2, 3). Although the Hertz model is most often used to estimate Young's modulus, its assumption of cells as an infinitely thick, purely elastic, isotropic and homogeneous material is inaccurate. It has been reported that the indentation depth is the critical parameter, because it reflects the largest errors arising from the variation in the contact point, noise fluctuation, and contact area (2). The absolute Young's modulus may not be reliable; however, comparison of relative differences in measurements taken under the identical conditions is reasonable. In our experiment, we recorded force plots with ramp sizes of 2 μm and 500 nm. Both sets of results show a range of estimated absolute Young's moduli of the cells. Fig. S3 shows a visible difference in Young's modulus between MCF-7/GFP and MDA-MB-436/RFP cells.

From a biochemical perspective, a plausible reason for the difference in cell stiffness is a difference in the structure of the cytoskeleton. Expression levels of F-actin, cytokeratin 18 (CK18), and vimentin are usually used to assess cytoskeletal deformability (4–6). Therefore, to confirm the basis of the mechanical difference between MCF-7/GFP and MDA-MB-436/RFP cells, we also stained the cells for F-actin, CK18, and vimentin and used the cytoskeleton data to characterize the mechanics of the two cell types.

Fluorescent Staining Shows the Difference in Cytoskeletal Protein Expression Between MCF-7/GFP and MDA-MB-436/RFP Cells. MCF-7/GFP and MDA-MB-436/RFP cells on four-chamber cell culture slides (BD Falcon) were immunostained with antibodies to cytoskeletal biomarkers. Cells were cultured on the slides for 48 h, fixed with 10% neutralized formaldehyde, and made permeabilized with 0.2% Triton-X 100 (Sigma) in PBS. Fixed cells were blocked with 5% horse serum (Sigma) in PBS and incubated with antibodies to CK18 (1:300; Abcam), and vimentin (1:300; Cell Signaling) at room temperature for 1 h. Cells were washed three times with PBS and incubated with secondary antibody conjugated to Alexa Fluor 647 (Invitrogen) for 1 h at room temperature. Nuclei were visualized with DAPI. To evaluate cytoskeletal structure, F-actin was stained with Rodamin-phalloidin in MCF-7/GFP, and with Alexa488-phalloiding in MDA-MB-436/RFP cells. Morphological characteristics, actin filament formation, and molecules of interest in the cells were observed, and all images were captured with confocal microscopes FV1000 (Olympus).

Fig. S4 shows the fluorescence images of labeled F-actin, CK18, and vimentin. For CK18 and vimentin staining, secondary antibodies conjugated to Alexa Fluor 647 (far-red) were used to prevent overlap of the emission signal with endogenous signals of GFP (green) and RFP (red). For each molecule, MCF-7/GFP and MDA-MB-436/RFP cells were stained in the same chamber slide and images were captured using the same settings to allow an accurate comparison. Negative control samples on each slide were incubated with mouse or rabbit IgG. Positive F-actin signals are shown in gray. The greater stiffness of MCF-7/GFP cells is indicated by the higher expression level of F-actin and CK18, and by the lower expression level of vimentin, compared with MDA-MB-436/RFP cells (4–6).

SI Results

SI Figures and Discussion of the MCF-7/GFP and MDA-MB-436/RFP Separation Experiment. Statistical analyses of cell size done on both cell samples before and after the separation experiment indicated that cell size changed minimally (less than 10% of mean values) during mechanical separated chip (MS-chip) separation (Fig. S7). Although the average size of MDA-MB-436 cells is slightly greater than that of MCF-7 cells, our separation data show that more MDA-MB-436 than MCF-7 cells crossed the post arrays. Based on these two observations, we concluded that cell size plays a minor role compared with deformability in MS-chip separation.

Expression analysis of adhesion marker RNAs showed that some markers (e.g., CD44 and β1 integrin) are overexpressed in the flexible cells released from the MS-chip, whereas others (e.g., CD24) are underexpressed, compared with levels in the stiff, captured cells. These data are shown in Dataset S1. In addition, in adhesion assays, cells are routinely incubated under undisturbed conditions for >1 h (7). Thus, cytoadherence is not likely to be a significant factor during the brief period (15 min) that motility is monitored in our experiments.

Analysis of FACS Data for SUM149 Cells Before and After Separation. Based on isotype control of CD44 and CD24 staining (Fig. S8), Fig. 5 *C* and *D* were created to indicate the populations $CD44^+/CD24^-$, $CD44^+/CD24^+$, $CD44^-/CD24^-$, and $CD44^-/CD24^+$.

Based on the data shown in Figs. S8–S10, the $CD44^{high}/CD24^-$ population is indicated in Fig. 5 *C* and *D*. However, it is still difficult to clearly delineate the $CD44^{high}$ population (shown in Fig. S9). Therefore, we used the established standard (8) and designated the far right section of the scatter plot $CD44^{high}$ We also indicate the $CD24^-$ population, which can be clearly defined based on isotype control of CD24 staining (Fig. S10). Application of these criteria allowed delineation of the $CD44^{high}/CD24^-$ population, as indicated by the red box in Fig. 5 *C* and *D*.

Optimization of Chip Design. Separation efficiency is highly correlated with the structural design of the post arrays. A number of microfluidic chip designs have been developed to achieve cell sorting based on cell size, cell type, surface biomarkers, and mechanics (9–11). Austin and colleagues (11, 12) demonstrated fractionation of white blood cells based on stretch-activated adhesion using arrays of short rectangular channels of varying width, as early as 1997. Mohamed et al. (13) used arrays of rectangular posts on-chip to retain circulating tumor cells (CTCs) in blood samples, based on the fact that CTCs are approximately >twofold as large as normal red blood cells (~7 μm). Separation of cancer cells of different sizes was also achieved by asymmetric bifurcation of laminar flow around obstacles in microfluidics devices, where the round posts were positioned slightly out of alignment (14, 15).

Based on these early studies in MS-chip design, we decided to use arrays of round posts because we believed the round edges would be less damaging to cells than rectangular edges. Toner and colleagues reported the isolation of CTCs with a chip design based on round posts. The captured CTCs were viable (10) after enrichment, providing support for the theory that round posts cause minimal damage to cancer cells. Because we did not want to introduce bias in terms of cell size, we used a matrix array of posts instead of misaligned array used in bifurcation separation (14, 15).

Based on the matrix array of round posts, we optimized the flow rate distribution and the cell separation throughput with three generations of devices. We varied the arrangements of the post arrays to guide the fluid flow direction, as shown in Fig. S12. Movie S5 shows the flow patterns of the cells in typical separation experiments using the earlier designs.

The first-generation design was used for mechanical cell separation and on-chip cell culture experiments (Fig. S12*A*). We found that stiff cells blocked the small (1,000 × 200 μm) area of the post array region and that improvement of throughput was required to obtain a sufficient number of cells for downstream phenotype study. Movie S5 shows the results of separation with this design.

We then attempted to improve throughput in the second-generation design (Fig. S12 *B*–*D*). However, because of the uneven distribution of flow through the zig-zagging channels of this type of chip, cells were unable to pass through the post array regions. Although the total resistance (pressure difference from the inlet to the outlet) for all possible routes of cell passage is similar, inertia prevents cells from entering post arrays, and cells are more likely to travel in a straight line than across arrays (Movie S5).

In the third generation, chips were designed to contain a higher density of post arrays. The design (Fig. S12 *E* and *F*; also see Fig. 1) provided very effective mechanical separation. Uniform flow rate distribution perpendicular to the direction of flow ensured a more uniform shear force on individual cells compared with earlier designs. We also used a series of decreasing gap sizes, instead of a single gap size, to increase efficiency of cell enrichment.

1. Kevin DC (2004) Single-cell elastography: Probing for disease with the atomic force microscope. *Dis Markers* 19(2):139–154.
2. Lekka M, Laidler P (2009) Applicability of AFM in cancer detection. *Nat Nanotechnol* 4 (2):72–72, author reply 72–73.
3. Lekka M, Laidler P, Rao JY, Gimzewski JK (2009) Applicability of AFM in cancer detection. *Nat Nanotechnol* 4(2):72–73, author reply 72–73.
4. Eckes B, et al. (1998) Impaired mechanical stability, migration and contractile capacity in vimentin-deficient fibroblasts. *J Cell Sci* 111(Pt 13):1897–1907.
5. Gardel ML, et al. (2004) Elastic behavior of cross-linked and bundled actin networks. *Science* 304(5675):1301–1305.
6. Beil M, et al. (2003) Sphingosylphosphorylcholine regulates keratin network architecture and visco-elastic properties of human cancer cells. *Nat Cell Biol* 5(9): 803–811.
7. Kim JB, et al. (2008) CD24 cross-linking induces apoptosis in, and inhibits migration of, MCF-7 breast cancer cells. *BMC Cancer* 8:118.
8. Liu H, et al. (2010) Cancer stem cells from human breast tumors are involved in spontaneous metastases in orthotopic mouse models. *Proc Natl Acad Sci USA* 107(42): 18115–18120.
9. Fu AY, Spence C, Scherer A, Arnold FH, Quake SR (1999) A microfabricated fluorescence-activated cell sorter. *Nat Biotechnol* 17(11):1109–1111.
10. Nagrath S, et al. (2007) Isolation of rare circulating tumour cells in cancer patients by microchip technology. *Nature* 450(7173):1235–1239.
11. Carlson RH, et al. (1997) Self-sorting of white blood cells in a lattice. *Phys Rev Lett* 79 (11):2149–2152.
12. Carlson RH, Gabel C, Chan S, Austin RH (1998) Activation and sorting of human white blood cells. *Biomed Microdevices* 1(1):39–47.
13. Mohamed H, Murray M, Turner JN, Caggana M (2009) Isolation of tumor cells using size and deformation. *J Chromatogr A* 1216(47):8289–8295.
14. Huang LR, Cox EC, Austin RH, Sturm JC (2004) Continuous particle separation through deterministic lateral displacement. *Science* 304(5673):987–990.
15. Hur SC, Henderson-MacLennan NK, McCabe ERB, Di Carlo D (2011) Deformability-based cell classification and enrichment using inertial microfluidics. *Lab Chip* 11(5): 912–920.

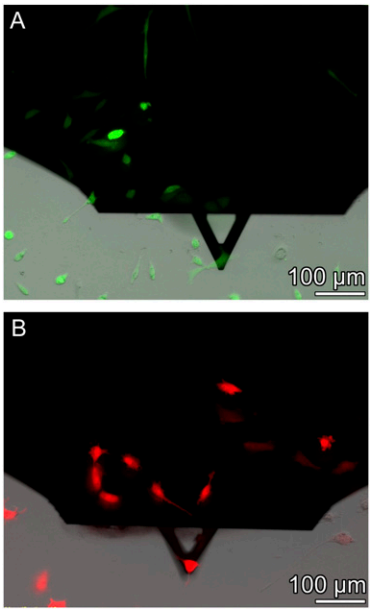

Fig. S1. Merged bright-field and fluorescence images showing AFM tips approaching (*A*) MCF-7/GFP and (*B*) MDA-MB-436/RFP cells. Cells under the cantilever are visible because the objective lens is able to effectively collect fluorescence scattering.

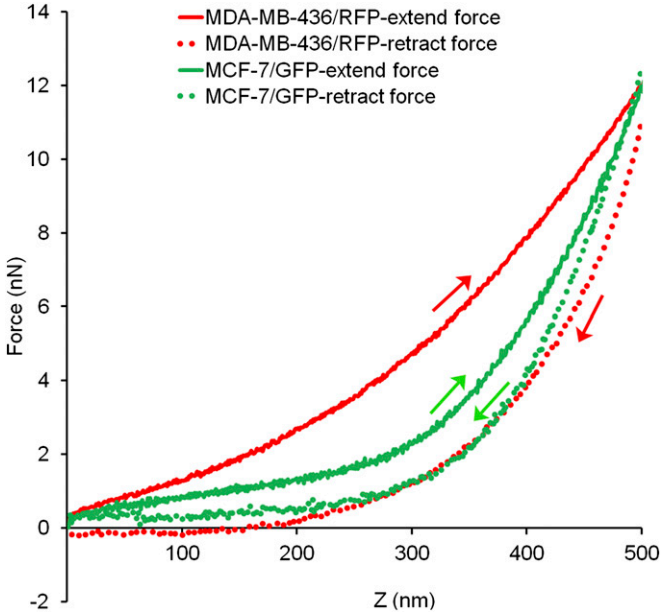

Fig. S2. Representative extend/retract force-distance curves are recorded from AFM indentation experiments on MCF-7/GFP (green curves) and MDA-MB-436/RFP (red curves) cells. Upward pointing arrows indicate approaching force and downward pointing arrows indicate retracting force.

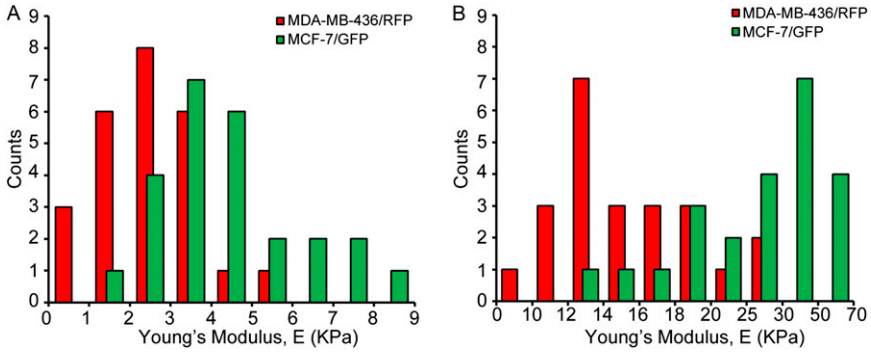

Fig. S3. Estimated Young's modulus for MCF-7/GFP and MDA-MB-436/RFP cells determined by AFM indentation. The histogram shows numbers of cells (counts) with measured Young's modulus collected from the two cell lines using (*A*) 2-μm ramp size and 2-μm/s ramp velocity and (*B*) 500-nm ramp size and 500-nm/s ramp velocity.

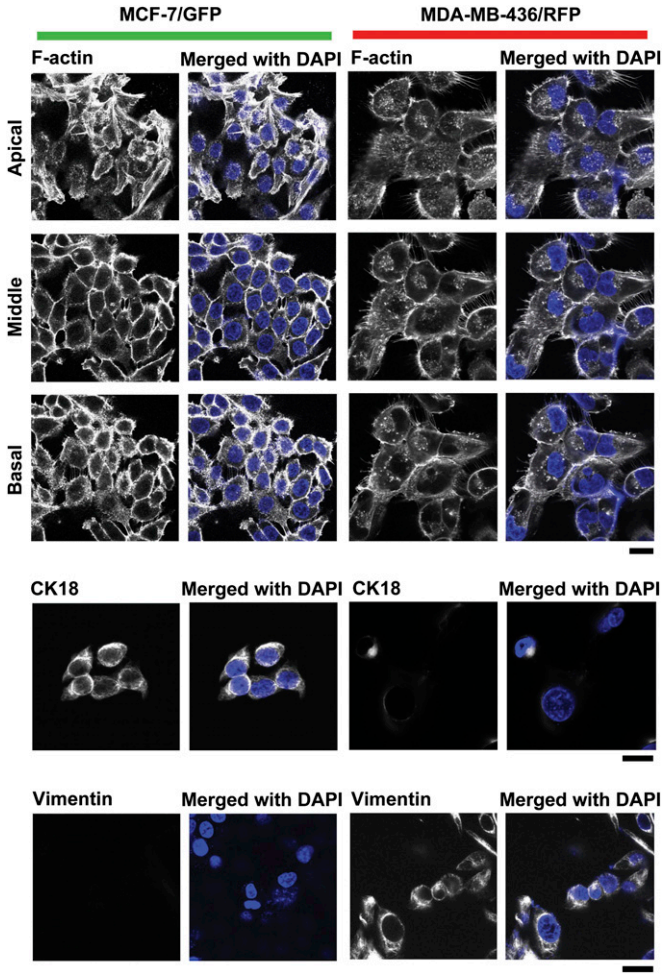

Fig. S4. Cytoskeletal staining of MCF-7/GFP and MDA-MB-436/RFP cells. Staining of F-actin, CK18, and vimentin in MCF-7/GFP (*Left*) and MDA-MB-436/RFP (*Right*) cells. Images of apical, middle, and basal aspects were taken for F-actin staining. DAPI (blue) was used to visualize the nuclei. (Scale bars, 20 μm, located in the bottom right corner of each panel.)

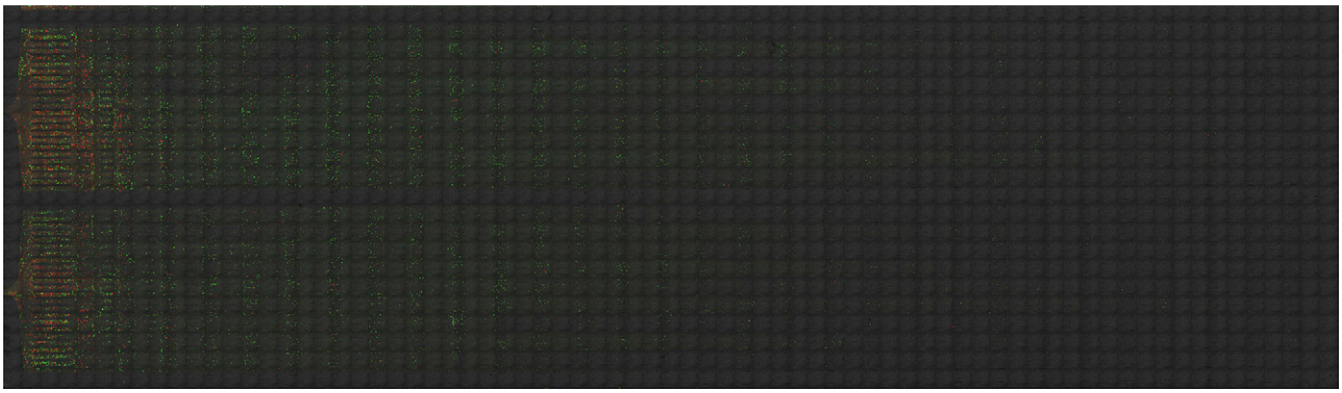

Fig. S5. High-resolution (16,852 × 4,832 pixels) image of two functional rows on an MS-chip. A stitched image composed of ~1,533 images (20× magnification; transmission detection/GFP/RFP merged) shows the distribution of MCF-7/GFP and MDA-MB-436/RFP cells on an MS-chip. All areas in this image can be "zoomed in" to clearly show the cells retained on the chip.

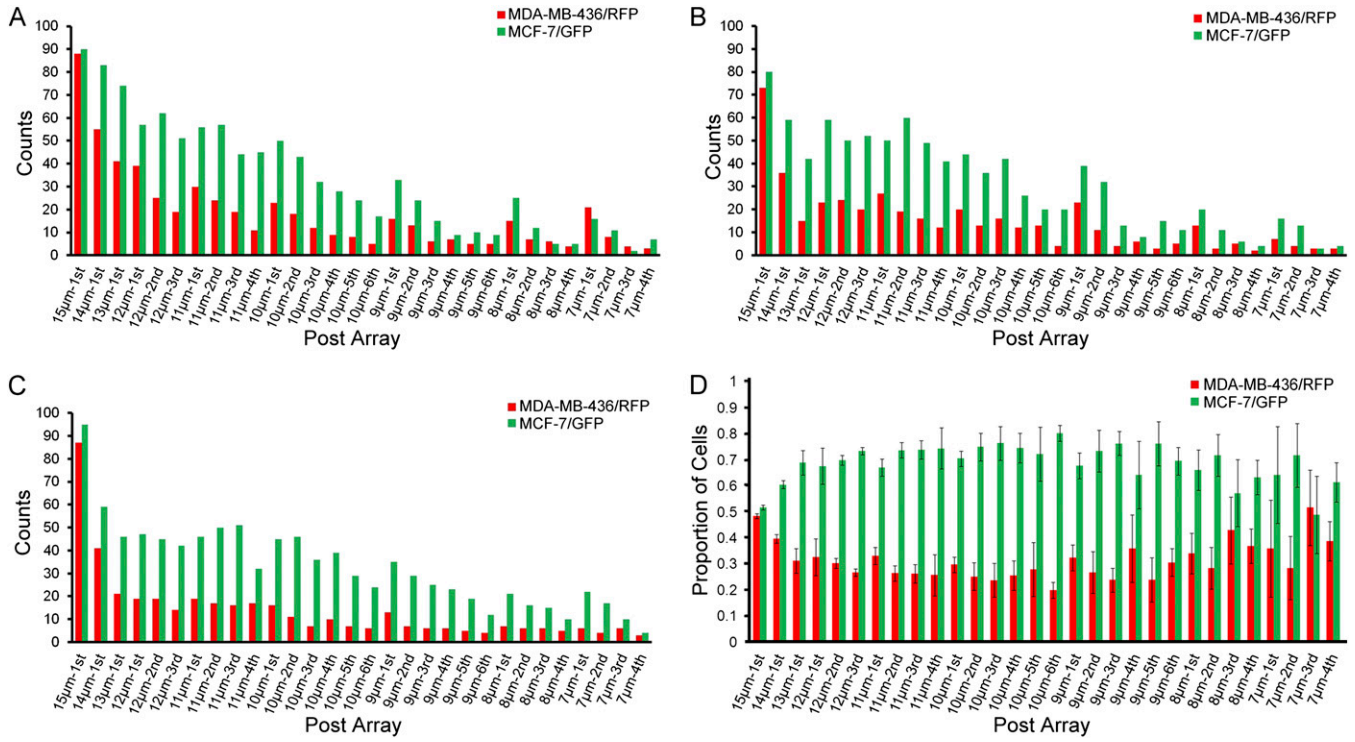

Fig. S6. Statistical analysis of cells retained on chip. (*A*–*C*) The numbers (counts) of MCF-7/GFP and MDA-MB-436/RFP cells from the 15-μm to 7-μm gap regions, from three independent experiments. (*D*) The proportion of MCF-7/GFP and MDA-MB-436/RFP cells captured on MS-chip from beginning to the end of the separation. Values represent mean ± SD and are based on the cell counts shown in *A*–*C*. The experiments were initiated with approximately equal amounts of MCF-7/GFP and MDA-MB-436/RFP cells, as indicated at the 15-μm gap at the front of the chip. The ratio of MCF-7/GFP to MDA-MB-436/RFP cells varied throughout the length of the chip, with the fewest MDA-MB-436/RFP cells being localized in the center of the chip.

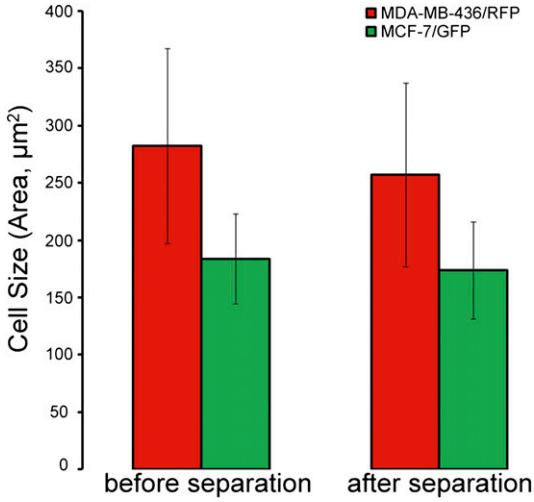

Fig. S7. Statistical analysis of cell size before and after separation via MS-chip. Red bars indicate MDA-MB-436/RFP cells and the green bars indicate MCF-7/GFP cells. A total of 432 cells were analyzed (114, 130, 87, and 92 cells from left to right bar). Values represent means ± SDs.

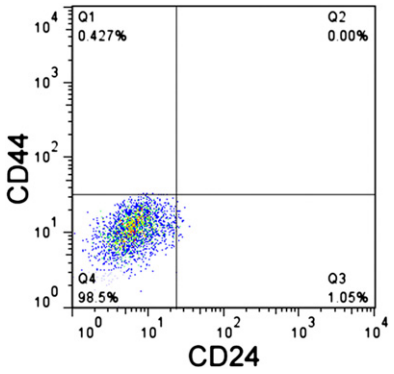

Fig. S8. Isotype control of CD44 and CD24 staining.

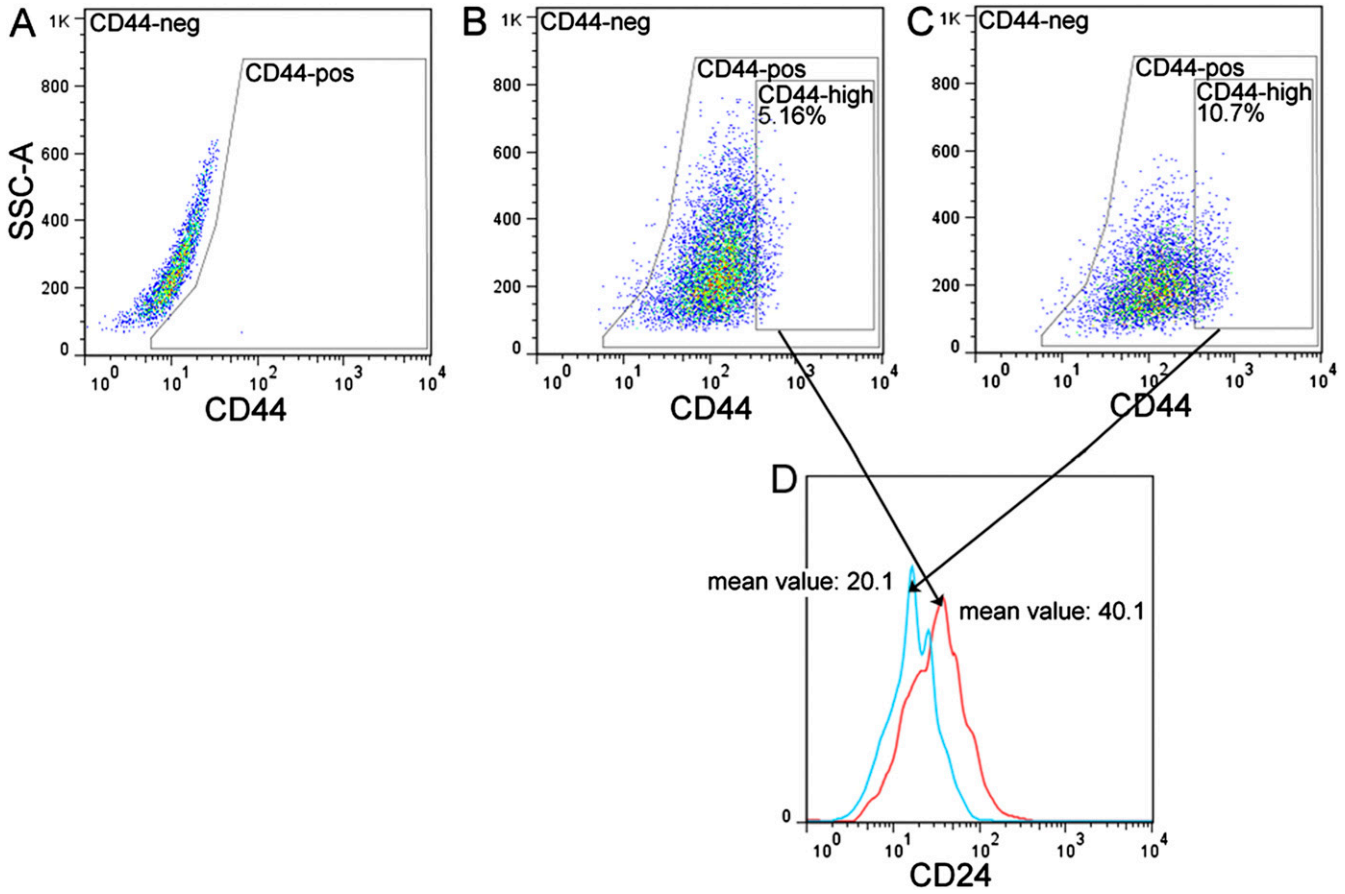

Fig. S9. (*A*) Isotype control of CD44 staining. (*B* and *C*) CD44 expression in parental SUM149 cells (*B*) and flexible SUM149 cells (*C*) after separation. The $CD44^{high}$ population is indicated on the right. An enrichment of the $CD44^{high}$ population is seen after MS-chip separation. (*D*) CD24 expression in $CD44^{high}$ populations of parental (blue) and flexible (red) SUM149 cells.

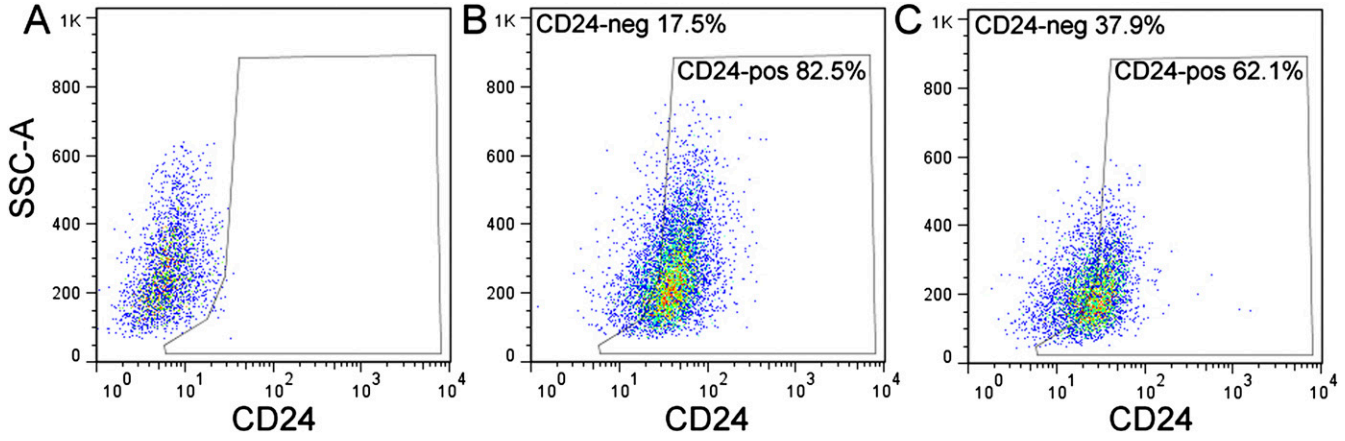

Fig. S10. (*A*) Isotype control of CD24 staining. (*B* and *C*) CD24 expression in parental SUM149 cells (*B*) and flexible SUM149 cells after separation (*C*). A twofold enrichment of the $CD24^{-}$ population is seen after MS-chip separation.

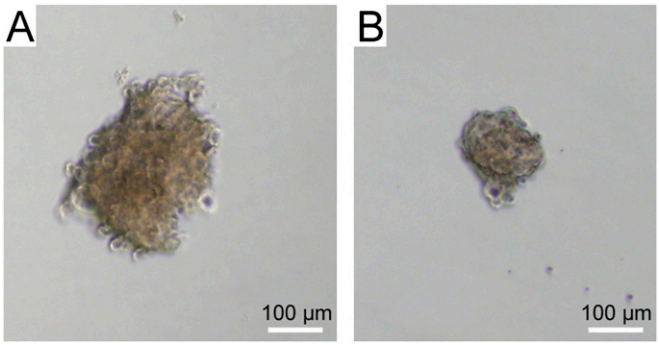

Fig. S11. Mammospheres derived from flexible and stiff SUM149 cells. Representative images show that mammospheres derived from flexible cells (*A*) grew larger than those formed by stiff cells (*B*), in agreement with the mammosphere formation efficiencies shown in Fig. 5*E*.

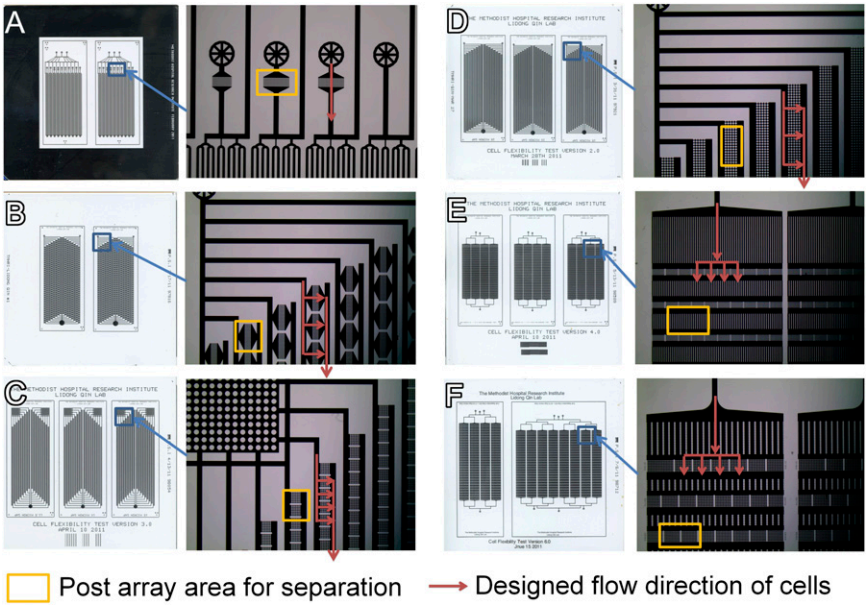

Fig. S12. Cell separation photomasks. Three generations of chip design have been tested to optimize the efficiency of mechanical separation of cancer cells. (*A*) First-generation design: separation-and-culture chips. (*B–D*) Second-generation design: zig-zagging flow-path chips. (*E* and *F*) Third-generation design: straight-flow path chips. Yellow boxes indicate the post array area and red arrows indicate the direction of flow. Areas boxed in blue and indicated by blue arrows on the left are shown at higher magnification in the respective panels immediately to the right.

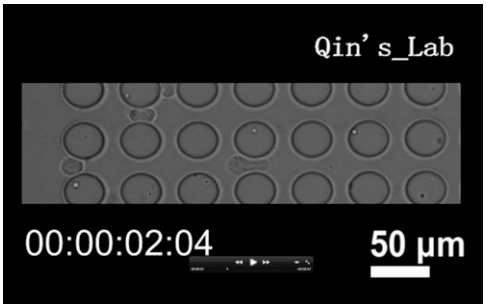

Movie S1. A real-time movie showing the distinctive behaviors of three cells with different mechanical properties in a MS-chip. (Magnification, 20×.)

Movie S1

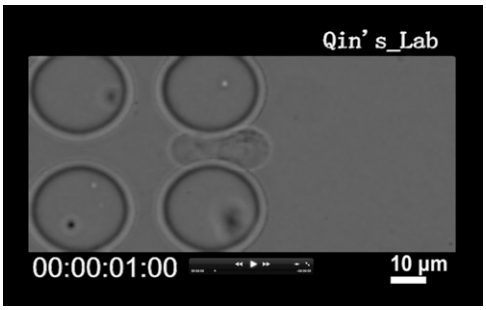

Movie S2. A real-time movie showing a single cell that deforms and crosses a gap between two posts. (Magnification, 40×.)

Movie S2

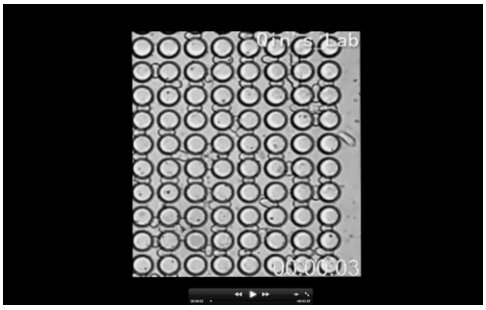

Movie S3. A real-time movie showing the cell-sorting process. (Magnification, 10×.)

Movie S3

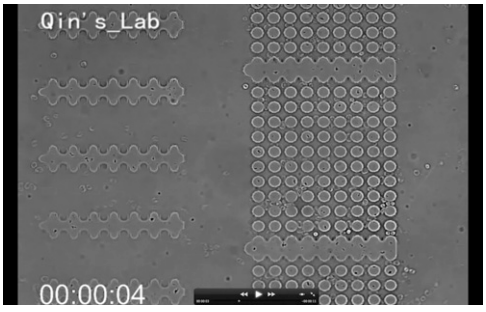

Movie S4. A real-time movie showing the lysis of retained cells in the post array of a MS-chip. (Magnification, 4×.)

Movie S4

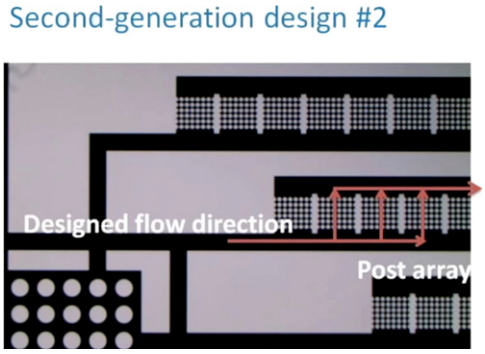

Movie S5. A movie collection showing the early generations of chip design.

Movie S5

Dataset S1. List of 288 genes overexpressed (>threefold change) in flexible vs. stiff SUM149 cells

Dataset S1 (XLSX)

Dataset S2. List of genes differentially expressed (<0.001 false-discovery rate) in flexible vs. stiff SUM149 cells

Dataset S2 (XLSX)